# Hydrodynamics of Damping Plates at Small *KC* Numbers

Haiping He[1,2], Armin W. Troesch[1], Marc Perlin[1]

[1] Dept. of Naval Architecture and Marine Engineering, University of Michigan, Ann Arbor, MI 48109, USA
[2] Presently at ExxonMobil Upstream Research Company, PO Box 2189, Houston, TX 77252, USA

The performance of circular thin plates in enhancing hydrodynamic damping of lightly damped offshore structures such as Spar Platforms and Tension Leg Platforms is studied. These platforms can experience resonant oscillations in heave under first and more likely second-order wave forces. As such, drag-augmenting devices are desired to limit the response amplitude to a safe range. This work includes two parts. The first part focuses on the damping coefficients' parametric dependence ($KC$ number) and geometric dependence (thickness-to-diameter ratio). The study exploits a series of forced oscillation experiments. The experiment spans a range of $KC$ numbers from 0.01 to 1.1 and a range of thickness-to-diameter ratios from 1/87.5 to 1/25. The second part of this study focuses on the underlying flow physics utilizing flow visualization experiments. The results of $KC$ number dependence indicate three $KC$ regimes where the damping coefficient behaves differently. Further flow visualization experiments demonstrate four unique vortex formation modes in these three $KC$ regimes. A comparison of the slopes of the damping curve indicates that the interaction of vortices generated from two half cycles increases the damping effectiveness. For plates with different thickness-to-diameter ratio, similar characteristics of $KC$ dependence are observed. The transitional $KC$ numbers are thickness-to-diameter ratio dependent with the transitions occurring at larger $KC$ numbers for thicker plates. While the total force experienced by oscillating plates is linear with $KC$ number and essentially independent of the thickness-to-diameter ratio, a significant reduction in damping with an increase in thickness-to-diameter ratio is observed.

## 1 Introduction

Offshore structures such as spar platforms and tension leg platforms may experience resonant oscillation in heave under first and more likely second-order wave forces; thus damping becomes a critical factor in limiting the

E. Kreuzer (ed.), *IUTAM Symposium on Fluid-Structure Interaction in Ocean Engineering*, 

response amplitude of the structures. Usually, these offshore structures are lightly damped; while the magnitude of the exciting force may be small, the response of the system may not be negligible due to very low damping in the system. As a result, damping-augmenting devices may be required to limit the response amplitude to a safe range. In the present research, thin plates are studied as one method to enhance the hydrodynamic damping. In typical applications, these plates are oriented horizontally along vertical structural members.

A damping plate can be modeled as a circular plate oscillating in its axial direction in a quiescent flow as shown in Figure 1. Two fundamental non-dimensional parameters for such flows are the Keulegan-Carpenter ($KC$) number and the $\beta$ number defined as follows:

$$KC = \frac{2\pi a}{L} (= S^{-1}) \tag{1}$$

$$\beta = \frac{L^2 f}{\nu} \tag{2}$$

where $L$ is a characteristic length, $S$ is the Strouhal number, $\nu$ is the kinematic viscosity, $f$ is the oscillation cyclic frequency, and $a$ is the amplitude of motion. There are two obvious choices for the characteristic length $L$, diameter, $D$ or thickness, $t$. In this work diameter is chosen as the characteristic length. Note that the product of these two dimensionless numbers, $KC$ and $\beta$, yields a Reynolds number. Since there are two length scales in the problem, the aspect ratio $t/D$, disk thickness-to-diameter is selected as the second dimensionless parameter.

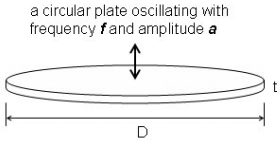


**Fig. 1.** Damping plate modelling

Although flow around oscillating bodies has been investigated previously, due to their broad engineering application much of the existing work is focused on cylinders. Relatively few studies have been conducted with circular plates. In a comprehensive survey, Dalzell[1] reviewed earlier research on forces experienced by oscillating plates. Included in this review were analyses of two sets of experiments on circular plates with the following parameters: thickness-to-diameter ratio of 1/32 and 1/40, $KC$ number range of 0.07 to

0.63, and $\beta$ number range of $6 \times 10^3$ to $4.8 \times 10^4$. These experiments were conducted using the decrement test method, which is problematic when the damping is highly $KC$ dependent[2]. As far as computations are concerned, De Bernardinis[3] calculated the unbounded oscillatory flow around a circular plate using a discrete vortex model. The flow around the disk edge is characterized by the formation of vortex pairs and their unidirectional self-induced motion and convection from the plate. His calculations for the drag coefficient,$C_d$, follow a $KC^{-1/3}$ trend for $KC$ numbers below 1.5; above this value, the results diverge rapidly from the $KC^{-1/3}$ trend. Thiagarajan[4] conducted flow visualization studies on both a disk with uniform thickness and a disk with a sharp beveled edge. The beveled disk had infinitesimal thickness (to machining accuracy) at the edge. His results demonstrated that the flow was anti-symmetric about the mean position of oscillation at large $KC$ number. Lake et al.[5] tested a circular plate with thickness-to-diameter ratio of 1/24. The experiment was conducted using the forced oscillation-at-resonance method initiated by Kim and Troesch.[6][7] An impressive damping increase for a thin disk was observed when compared to axially oscillating cylinders of the same diameter. Tao[8] examined numerically the flow patterns around the disk edges of a cylinder-disk configuration using a finite difference method. Three distinct vortex patterns were observed near the edges of the disks. As can be seen the present understanding of the hydrodynamics of oscillating thin plates is limited and preliminary, especially with regard to the flow physics contributing to the hydrodynamic damping effectiveness. This work first investigates hydrodynamic damping's dependence on $KC$ number by using force measurement experiments. Then, the vortical flow patterns contributing to different damping regimes are identified by conducting a series of flow visualization experiments. The flow visualization leads to better understanding of the flow physics that cause increased hydrodynamic damping. The first part of this paper contains the engineering motivation that is necessary to establish and connect the regimes addressed in the latter part where the relevant flow physics are described.

## 2 Hydrodynamic Force Modells

Consider a circular plate oscillating axially in a quiescent liquid. The hydrodynamic force can be modeled as an added mass (i.e. increased system inertia) and a damping force (i.e. system energy dissipation). Two popular choices for the damping force are an equivalent linear representation and a velocity-squared Morison's equation representation.[9] Since the limiting behavior of $C_d$ for a disk as $KC$ approches to 0 is not well defined (e.g. in some models it is singular, Lake et al., 2000), mathematically it is more reasonable to use a linear damping model. The added mass ($A$) and damping ($B$) coefficients are non-dimensionalized as $A'$ and $B'$, respectively, where

$$A' = \frac{A}{m} \tag{3}$$

$$B' = \frac{B}{2m\omega} \tag{4}$$

Here, $m = \frac{1}{3}\rho D^3$ is the theoretical ideal-fluid added mass for a flat disk of diameter $D$ and angular frequency $\omega$ $(2\pi f)$. Morison's drag coefficient, $C_d$, can be expressed in terms of $B'$ as:[10]

$$C_d = \frac{4\pi B'}{KC} \tag{5}$$

## 3 Experimental Setup and Techniques

Experiments are conducted at the MHL (Marine Hydrodynamics Laboratory) of the University of Michigan. A schematic of the experimental setup for the force measurements is shown in Figure 2. A vertically mounted shaker capable of producing periodic sinusoidal motion is used to force the oscillation. The shaker is an Unholtz-Dickie (UD) Model 20 Shaker with a UD Model TA100A Solid State Power Amplifier, capable of oscillating the disk in the vertical direction at a frequency to 5.0kHz with a maximum one inch (2.54cm) peak-to-peak oscillation amplitude and 250 lbs. (1103N) peak-to-peak force. The experiments were conducted in a stationary tank sufficiently large so as to avoid the hydrodynamic interaction between the model, the tank walls and the water surface. The surface area of the tank is 5.67ft 3.17ft (1.73m 0.97m) and the water depth is 4.0ft (1.22m). Two load cells, a linear variable displacement transducer (LVDT), and a piezoelectric accelerometer are used to measure the heave response force, the vertical displacement, and the vertical acceleration, respectively. The accelerometer is used primarily to verify the output from the LVDT. The output from these instruments is amplified and subsequently filtered using low-pass Butterworth filters with a cutoff frequency of 40 Hz (10 times the forcing frequency). The filtered data signals are sampled and acquired by a National Instrument data acquisition board (DAQ) with a sample rate of 1024Hz. Sixty-four cycles of data are recorded during a typical run. These data are then Fourier analyzed to identify the magnitude and phase of the force and displacement. The phase shift due to the filters (and the DAQ board) is calibrated before each experiment and a correction is made. A typical phase correction is 22 degrees at 4 Hz. A DELL® PC is used to conduct the data acquisition and analysis. For the flow visualization experiment, images are acquired by a Kodak Ektapro 1012 high speed video imager, which has a resolution of $239 \times 192$ pixels. A typical cross-sectional field of view is $0.96in \times 0.77in$ $(24.3mm \times 19.5mm)$. The imager has built-in memory capable of storing 409 frames and its recording rate is to 1000 frames/second. Conduct-O-fil® particles with 13 $\mu m$ mean diameter are used to track the flow with a 5-watt Argon-ion laser used to illuminate the flow.

A computer program written in Labview® is used to control and synchronize the oscillation of the disk and the operation of the imager. In a typical flow visualization, the exposure time of the camera is set sufficiently long to record the trajectory of the moving particles. Two sets of lenses are used to obtain the desired magnification and depth of field.

Three aluminum disks with diameter of 7 inch (177.8mm) and thickness-to-diameter ratios of 1/87.5, 1/37, and 1/25 are oscillated at 4 Hz ($\beta = 1.24 \times 10^5$). The $KC$ number ranged from 0.01 to 1.1. Both the force measurement and flow visualization results are presented in the following section.

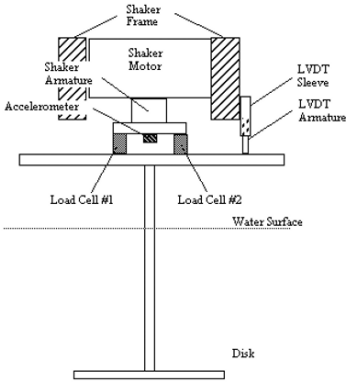


**Fig. 2.** Schematic of the forced oscillation experimental setup

## 4 Experimental Results

The $KC$ ($=S^{-1}$) number represents the amplitude of fluid motion, or the amplitude of disk motion in the present case, relative to the diameter of the disk. The magnitude of the $KC$ number indicates the relative importance of drag to inertia force. At low $KC$ numbers, the inertia force dominates the flow. With an increase of $KC$, the drag force due to flow separation becomes more important. Figure 3 shows damping coefficient as a function of $KC$ number ($KC$ from 0.01 to 1.1) for the disk with thickness-to-diameter ratio of 1/87.5. Each data point is based on a Fourier analysis of 64 cycles of oscillation. An examination of the damping curve shows that there are two slope discontinuities at $KC$ numbers around 0.075 and 0.13, thus separating the damping curve into three $KC$ regimes. There is an apparent small zero-$KC$-number offset. It is hypothesized that the damping curve's offset is due to friction drag, while the slope is due to form drag[4]. This agrees well with Tao's numerical results[8] which showed $KC$-independent damping at very low $KC$ number.

To understand the physics behind the damping trend, a series of flow visualization experiments are conducted by varying $KC$ numbers. As a result

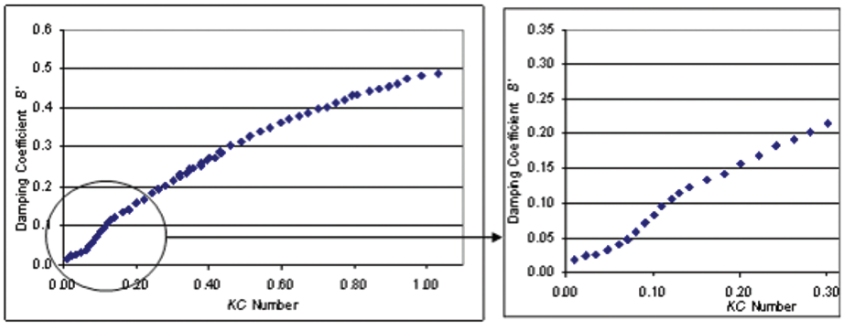


**Fig. 3.** Damping coefficients versus $KC$ number (t/D=1/87.5)

of the amplitude variation, four unique vortex formation modes are observed. The first mode is restricted to very small $KC$ number, a region where the present force measurement experimental technique is unable to resolve the damping force accurately. The next three damping coefficient regions can be characterized by three different vortex flows. Transitional flows are also observed. The vortex formation Modes 1 (independent vortex mode I) and 2 (independent vortex mode II) occur in the first $KC$ regime; Mode 3 (interactive vortex type I) and Mode 4 (interactive vortex type II: unidirectional shedding mode) occur at the second and third regimes respectively.

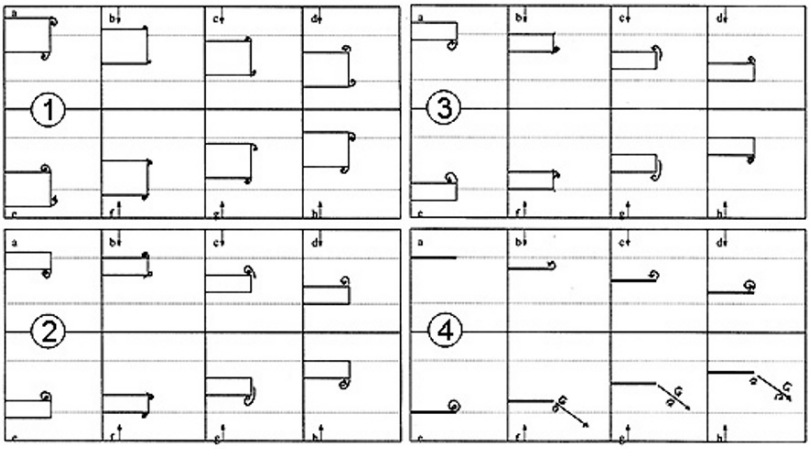


**Fig. 4.** Schematics of vortex formation modes. Note: the thickness is the same in all figures; the schematic is rescaled to show flow details.

For each vortex formation mode, a characteristic $KC$ number is selected and its corresponding vortex mode is presented. Figure 4 shows schematic

diagrams of the four vortex formation modes. For each mode, eight sketches are spaced equally through one period at 45 degree increments. The schematics are rescaled to exhibit flow details. Figure 5 shows the flow visualization results for the last vortex formation mode. For each run, eight sub-images are spaced equally in time through a cycle of oscillation, with the first sub-image in each figure showing the disk at the top dead position. The characteristics of four vortex formation modes are described as follows:

**Mode 1 (independent vortex type I, Figure 4-1, $KC = 0.016$)**

When the oscillation amplitude is much smaller than the disk thickness, the vortices generated from two disk edges never interact. Starting from the top dead phase T0, two small vortices exist around the two disk edges, with one at the bottom of the lower disk edge and the other along the right side of the top disk edge (Figure 4-1.a). As the disk reverses direction and moves downwards, both vortices are driven toward the other side edges, and at the same time lose strength. Concurrently, two vortices with negative vorticity (i.e. counter-clockwise) are generated around the other sides of the disk edges (Figure 4-1.b). These two vortices increase in strength until the disk reaches the lowest position of the motion (Figure 4-1.e). As the disk reverses direction, the same edge flow as the previous half cycle is observed (Figure 4-1.f to 4-1.h). The overall flow is symmetric about the mean oscillation position between two half-cycles, and is replicated from cycle to cycle with minimal cycle-to-cycle variation.

**Mode 2 (independent vortex type II, Figure 4-2, $KC = 0.049$)**

Starting from the first phase, top dead phase T0, a strong positive vortex (i.e. clockwise) can be seen below the lower disk edge generated from the previous cycle (Figure 4-2.a). As the disk reverses direction and moves downward, the vortex below the disk is driven towards the edge of the disk and simultaneously loses strength. Concurrently, two vortices with negative vorticity are generated around both edges of the disk, as shown in (Figure 4-2.b). As the disk continues its down-stroke, the two newly generated vortices come into contact and interact, and develop into one stronger vortex increasing in strength until the disk reaches its dead bottom position, as shown in (Figure 4-2.e). Due to the presence of the vortex, the flow at the edge reverses ahead of the ambient flow, as observed by Graham[11]. As the disk begins its up-stroke, the negative vortex above the disk is driven towards the edge of the disk and loses strength (Figure 4-2.f). Another two positive vortices are seen at the two edges of the disk (Figure 4-2.g) and repeat the vortex flow patterns of the previous half cycle with different vortex direction. It is noticed that the vortices generated off one side of the disk along the first half cycle are almost symmetric to that generated off the other side of the disk during the next half cycle. As in Mode 1, cycle-to-cycle variation is small.

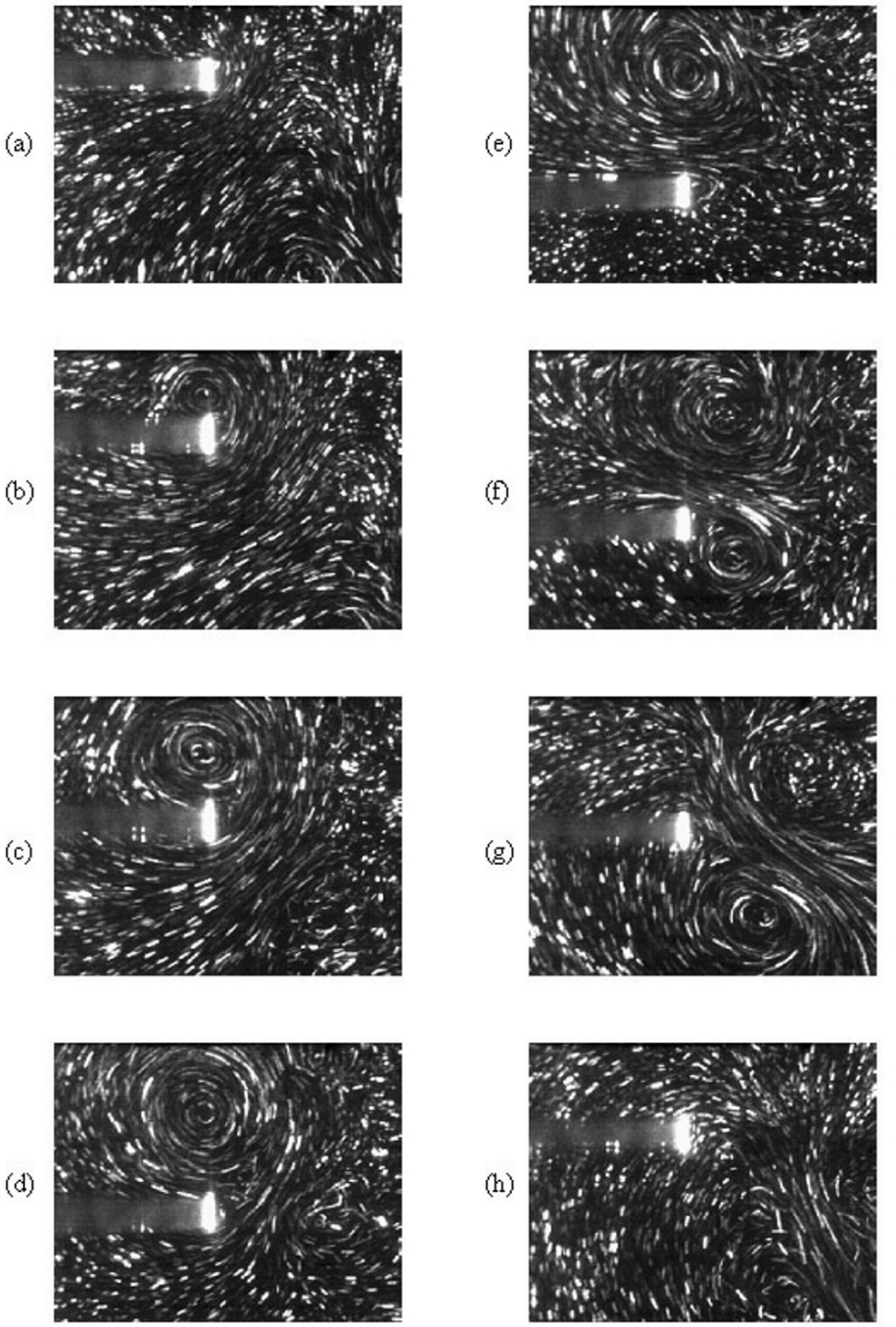


**Fig. 5.** Vortex formation mode 4 ($KC$=0.16, t/D=87.5). (a) top dead center. (a)-(h) spaced equally through one cylce of oscillation.

**Mode 3 (interactive vortex type I, Figure 4-3, $KC = 0.102$)**

Similar to Mode 2, a strong positive vortex below the bottom disk edge is generated from the last cycle at time T0 (Figure 4-3.a). As the disk reverses direction and moves downward, the vortex below the disk is driven towards the edge of the disk and begins to lose strength (Figure 4-3.b). At the same time, one vortex with negative vorticity (i.e. counter clockwise) is generated at the side surface of the disk due to the disk bottom edge, as shown in (Figure 4-3.b). In contrast to Mode 2, the strength of the decaying vortex is much larger than the same vortex in Mode 2 and it merges with and enhances the newly generated negative vortex. Clearly, the strength of the vortex plays an important role here. The second vortex at the top is relatively weak and barely visible. This is different from Mode 2, in which two vortices with approximately equal strength are generated from both edges of the disk.

As the disk continues its down-stroke, the newly generated vortex increases in strength until the disk reaches its dead bottom position, as shown in (Figure 4-3.e). As the disk begins its up-stroke, the same pattern of vortex generation is observed. Interestingly, the vortex generation pattern is still symmetric to that generated off the other side of the disk during the last half cycle. Cycle-to-cycle variations are observed during the experiment. Another distinct feature of this Mode is that the vortices generated from the down-stroke and up-stroke begin to interact with each other and result in an increased slope of the damping curve.

**Mode 4 (interactive vortex type II: unidirectional vortex shedding, Figure 4-4, $KC = 0.160$)**

Starting from the top dead position (Figure 5a, Figure 4-4.a), the strong positive vortex below the disk is not visible as in Modes 2 and 3. As the disk moves down, the edge vortices begin to "roll-up" from the disk edges and amalgamate into one negative vortex (Figure 5b, Figure 4-4.b). As the disk continues its down-stroke, the vortex strength is increased and it remains above the disk until the disk reaches the bottom (Figure 5c, d, e, Figure 4-4.c, d, e). As the disk reverses direction and moves upward, the vortex above the disk is driven towards the edge of the disk. Similar to Mode 3, the vortex does not lose its strength when it reaches the edge of the disk (Figure 5f, Figure 4-4.f). At the same time, a positive vortex is generated at the disk edge where it is enhanced by the interaction between the negative vortex and the disk (Figure 5f). Rather than rolling to the bottom of the disk, as was described for Modes 2 and 3, this positive vortex is drawn by the first negative vortex and forms a vortex pair (Figure 5g, Figure 4-4.g). The vortex pair causes a self-induced motion from the disk at a particular shedding angle with the up-stroke of the disk (Figure 5h, Figure 4-4.h). This unidirectional vortex pairing process repeats with each cycle of oscillation. The overall vortex shedding patterns

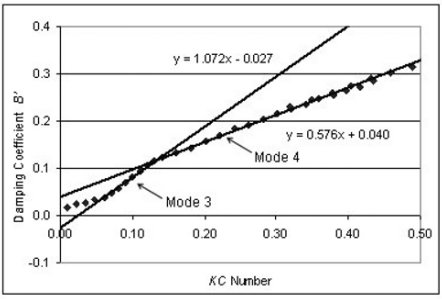


**Fig. 6.** Damping curve slopes of vortex mode 3 and mode 4. (The damping curve slope of mode 3 is approximately twice that of the curve of mode 4.)

repeat from cycle to cycle. However, dissimilarities in shedding trajectory and vortex size are observed from cycle-to-cycle during the experiment.

As can be seen from Figure 3, the damping curve slope of Mode 4 is significantly smaller than Mode 3. Comparing vortex Mode 3 with Mode 4, the vortices generated from the down-stroke and up-stroke begin to interact in both modes. However, in Mode 3, both the down-stroke and up-stroke are generating and developing new vortices, while in Mode 4, only the down-stroke is developing a vortex. The influence of the vortex dynamics on damping is seen in the damping curve slope of Mode 3 where it is approximately twice that of the curve of Mode 4 as shown in Figure 6, indicating a relative increase in damping effectiveness for unit increase in $KC$ number due to vortex interaction over the complete cycle.

A transitional region between Mode 3 and Mode 4 is also observed during the experiment. Generally, the negative vortex increases in strength as the disk moves downward. When the disk begins its upward movement, the positive vortex is generated. The shedding of the negative vortex prevents the positive vortex from rolling to the disk lower surface. However, unlike Mode 4, the first vortex is not sufficiently strong to coerce the second vortex to form the vortex pair; rather it is canceled by the second vortex. An anti-symmetric vortex pattern is seen during this transitional region.

Figure 7 shows the thickness-to-diameter ratio effect on the damping and the drag coefficient. From the damping curves, it can be seen that the 1/37 and 1/25 disks exhibit the same trend as the 1/87.5 disk. The difference is that two slope discontinuities appear at different $KC$ numbers and the transition from Mode 3 to Mode 4 of thick disks is not as obvious as for thin disks. At small $KC$ numbers, there is a significant reduction in $B'$ with an increase in thickness-to-diameter ratio (or with the increase in disk thickness). For example, at a $KC$ number of 0.3, the damping coefficients, for thickness-to-diameter ratios of 1/87.5, 1/37, and 1/25 are 0.21-0.22, 0.11-0.12, and 0.07-0.08, respectively. This represents a reduction in damping by a factor of three. The three damping curves are almost parallel to each other when the $KC$

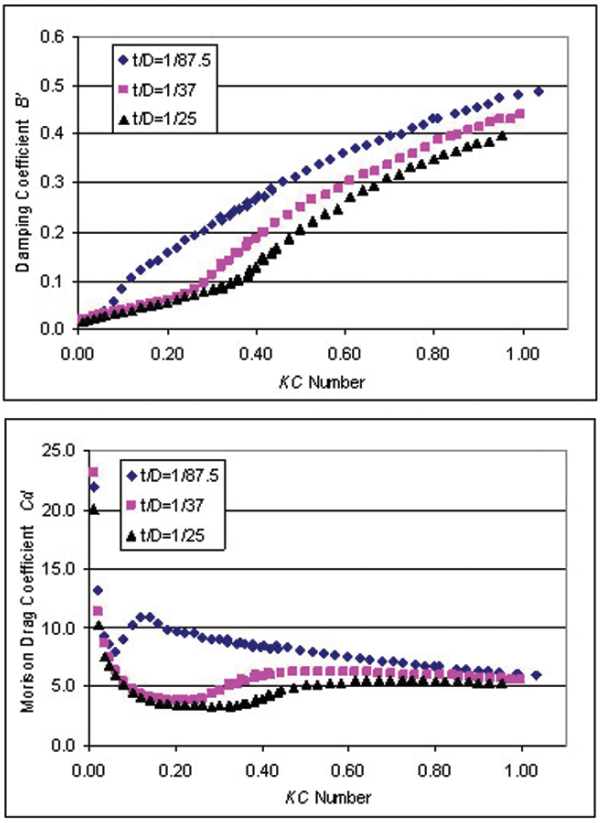


**Fig. 7.** Aspect ratio effect: (top) damping, and (bottom) drag coefficients.

number is larger than 0.4 and the absolute difference decreases. At *KC* number 0.6, the damping coefficients, for the aspect ratios 1/87.5, 1/37, 1/25 are 0.36, 0.30, and 0.26, respectively. This represents a reduction in damping by a factor of 1.4. It is known from the *KC* dependence investigation that the interaction of vortices generated from two disk corners and the interaction of the vortices generated from the up-stroke and down-stroke lead to four distinct vortex formation modes, resulting in distinct damping curve regimes. Apparently, these interactions are not only dependent on *KC* number, but also on disk thickness, or the ratio of oscillation amplitude to the thickness. On one hand, the thickness changes the *KC* number at which the vortices generated from the two corners begins to interact. On the other hand, the thickness influences the strength of the individual vortex and its ability to interact with previously generated vortices. An increase of thickness results in a decrease of vortex strength and a delay of the transition to the new vortex formation mode.

## 5 Conclusions

For oscillating thin plates, both $KC$ number and thickness-to-diameter ratio have significant influence on hydrodynamic damping. A significant reduction in damping is observed as thickness-to-diameter ratio increases. The underlying flow physics investigation demonstrates that the interaction of vortices generated from two half cycles plays a key role in damping effectiveness. On one hand, the interaction can enhance the vortex strength on both half cycles, which leads to an increase in damping effectiveness as seen in vortex Mode 3. Conversely, the interaction can result in uni-directional shedding of vortex pair and reduction of vortex generation in a full cycle and damping effectiveness as seen in vortex Mode 4.

## References

1. J. F. Dalzell (1978) Non-linear forces on oscillating plates: review and analysis of the literature. Stevens Institute of Technology, Davidson Laboratory, Hoboken, NJ, Report SIT-DL-78-9-2031
2. O. M. Faltinsen (1990) Sea loads on ships and offshore structures, Cambridge Univ. Press, Cambridge
3. B. De Bernardinis, J.M.R. Graham, and K. H. Parker (1981) Oscillatory flow around disks and through orifices, Journal of Fluid Mech., Vol. 102, pp. 279-299
4. K. P. Thiagarajan (1993) Hydrodynamics of flows past disks and circular cylinders, Ph.D. Dissertation, Dept. Naval Arch. and Marine Engineering, University of Michigan
5. M. Lake, H. He, A. W. Troesch, M. Perlin, K. P. Thiagarajan (2000) Hydrodynamic coefficient estimation for TLP and spar platforms, Journal of Offshore Mechanics and Arctic Engineering, vol. 122, May, pp. 118-124
6. S. Kim, and A. W. Troesch (1989) Streaming flows generated by high frequency-small amplitude oscillations of arbitrarily shaped cylinders, Physics of Fluids A, Vol. 1, No. 6, June, pp. 975-985
7. A. W. Troesch, and S. Kim (1991) Hydrodynamic forces acting on cylinders oscillating at small amplitudes, Journal of Fluids and Structures, Vol. 5, pp. 189-199
8. L. Tao, and K. Thiagarajan (2003) Low KC flow regimes of oscillating sharp edges, Applied Ocean Research, Vol. 25 p21-35, Vol. 25 p53-62
9. T. Sarpkaya, and M. Isaacson (1981) Mechanics of wave forces on offshore structures, van Nostrand Reinhold Co., New York
10. H. He (2003) Hydrodynamics of thin plates, Ph.D. Thesis, University of Michigan, Ann Arbor
11. J. M. R. Graham (1980) The forces on sharp-edged cylinders in oscillatory flow at low Keulegan-Carpenter numbers, Journal of Fluid Mech., Vol. 97, Part1, pp. 331-346